

AperTO - Archivio Istituzionale Open Access dell'Università di Torino

Characterization of a neutron imaging setup at the INES facility

This is the author's manuscript

Original Citation:

Availability:

This version is available <http://hdl.handle.net/2318/137805> since 2016-07-04T11:26:14Z

Published version:

DOI:10.1016/j.nima.2013.05.074

Terms of use:

Open Access

Anyone can freely access the full text of works made available as "Open Access". Works made available under a Creative Commons license can be used according to the terms and conditions of said license. Use of all other works requires consent of the right holder (author or publisher) if not exempted from copyright protection by the applicable law.

(Article begins on next page)



UNIVERSITÀ DEGLI STUDI DI TORINO

This is an author version of the contribution published on:

Questa è la versione dell'autore dell'opera:

*E.A. Durisi, L. Visca, F. Albertin, R. Brancaccio, J. Corsi, G. Dughera,
W. Ferrarese, A. Giovagnoli, N. Grassi, F. Grazzi, A. Lo Giudice, G. Mila, M. Nervo,
N. Pastrone, F. Prino, L. Ramello, A. Re, A. Romero, R. Sacchi, F. Salvemini, A.
Scherillo, A. Staiano,*

*“Characterization of a neutron imaging setup at the INES facility”,
Nuclear Instruments and Methods in Physics Research A 726 (2013) 31-36
DOI 10.1016/j.nima.2013.05.074*

The definitive version is available at:

La versione definitiva è disponibile alla URL:

<http://www.journals.elsevier.com/nuclear-instruments-and-methods-in-physics-research-section-a-accelerators-spectrometers-detectors-and-associated-equipment>

1 CHARACTERIZATION OF A NEUTRON 2 IMAGING SETUP AT THE INES FACILITY

3 E. A. DURISI^{1,2*}, L. VISCA^{1,2}, F. ALBERTIN², R. BRANCACCIO², J. CORSI^{1,2},
4 G. DUGHERA², W. FERRARESE^{1,2}, A. GIOVAGNOLI³, N. GRASSI³, F.
5 GRAZZI⁴, A. LO GIUDICE^{1,2}, G. MILA^{1,2}, M. NERVO³, N. PASTRONE², F.
6 PRINO², L. RAMELLO^{5,2}, A. RE^{1,2}, A. ROMERO^{1,2}, R. SACCHI^{1,2}, F.
7 SALVEMINI⁴, A. SCHERILLO^{4,6}, A. STAIANO²

8 ¹*Università di Torino, Dipartimento di Fisica, Via Pietro Giuria 1, 10125 Torino, Italy*

9 ²*Istituto Nazionale di Fisica Nucleare – Sezione di Torino, Via Pietro Giuria 1, 10125 Torino,*
10 *Italy*

11 ³*Fondazione Centro per la Conservazione ed il Restauro dei Beni Culturali “La Venaria Reale”,*
12 *Piazza della Repubblica, 10078 Venaria Reale (Torino), Italy*

13 ⁴*Consiglio Nazionale delle Ricerche, Istituto dei Sistemi Complessi, Via Madonna del Piano 10,*
14 *50019 Sesto Fiorentino (Firenze), Italy*

15 ⁵*Università del Piemonte Orientale, Dipartimento di Scienze e Innovazione Tecnologica, Viale*
16 *Teresa Michel 11, 15121 Alessandria, Italy*

17 ⁶*Science and Technology Facility Council, ISIS Neutron Source - Didcot, United Kingdom*
18

19 **Corresponding author at: Università di Torino, Dipartimento di Fisica, Via Pietro Giuria 1,*
20 *10125 Torino, Italy, Phone: +390116707954, Fax: +390116707020*
21 *e-mail address: elisabettaalessandra.durisi@unito.it*

22 ABSTRACT

23 The Italian Neutron Experimental Station (INES) located at the ISIS pulsed neutron source
24 (Didcot, United Kingdom) provides a thermal neutron beam mainly used for diffraction analysis.
25 A neutron transmission imaging system was also developed for beam monitoring and for aligning
26 the sample under investigation. Although the time-of-flight neutron diffraction is a consolidated
27 technique, the neutron imaging setup is not yet completely characterized and optimized. In this
28 paper the performance for neutron radiography and tomography at INES of two scintillator screens
29 read out by two different commercial CCD cameras is compared in terms of linearity, signal-to-
30 noise ratio, effective dynamic range and spatial resolution. In addition, the results of neutron
31 radiographies and a tomography of metal alloy test structures are presented to better characterize
32 the INES imaging capabilities of metal artifacts in the cultural heritage field.

33 *Keywords: Neutron imaging; Metal alloy; Cultural heritage*

34 1. Introduction

35 Analysis techniques based on thermal and epithermal neutrons represent a
36 powerful tool to characterize metal alloy artifacts in the cultural heritage field.
37 Neutrons are a non-invasive diagnostic tool and can penetrate thick layers of
38 samples. Neutron transmission imaging, obtained with radiographic or

39 tomographic techniques, allows to investigate the inner structure of artworks,
40 determining, as an example, the materials thickness and the conservation
41 condition [1, 2]. All this information can be helpful to assist restoration activities,
42 to increase the knowledge of the work of art and to help dating or attributing an
43 artifact through the understanding of the manufacturing techniques used.

44 The Italian Neutron Experimental Station (INES) is a neutron diffractometer
45 located at the ISIS pulsed neutron source [3]. A low-cost imaging device is
46 currently installed and used for beam monitoring and samples positioning.
47 Preliminary measurements were performed by Bartoli et al. [4] to test the imaging
48 setup. Salvato et al. realized an upgrade of the system providing the first neutron
49 tomography investigation at INES [5].

50 The aim of this paper is to fully characterize the present imaging setup in terms of
51 linearity, signal-to-noise ratio, effective dynamic range and spatial resolution. A
52 comparison with a different converter screen and a different CCD camera will be
53 shown. Moreover, the analysis of neutron radiography and tomography of metal
54 alloy test structures will be presented in order to assess the diagnostic potential of
55 the INES imaging apparatus on metal artifacts in the cultural heritage field.

56

57 **2. Experimental set up**

58 The Italian Neutron Experimental Station, INES, provides a stable pulsed neutron
59 beam with an approximately uniform intensity distribution over a cross section, at
60 the sample position, of $35 \times 35 \text{ mm}^2$ ($40 \times 40 \text{ mm}^2$ including also non-uniform
61 borders). The divergence of the beam, in terms of L/D ratio, is about 90.

62 The neutron imaging setup currently installed consists of a scintillator converter
63 screen, a mirror and a commercial CCD camera [6]. The scintillator is made of
64 $\text{ZnS}^{60}\text{LiF}$, 225 μm thick, layered on an aluminum substrate; in the following we
65 will refer to it as scintillator 1. It is positioned orthogonal to the incident neutron
66 beam, at a distance from the sample ranging from 1 cm to 10 cm and it emits
67 visible light centered at a wavelength of about 520 nm, in order to best match the
68 CCD sensitivity curve. A mirror reflects the emitted light toward a black and
69 white camera (The Imaging Source DMK21BF04) equipped with an optical
70 system of $f=16\text{mm}$ and $F/1.4$. The camera works at room temperature without any
71 image intensifier and is based on a Sony ICX098BL CCD sensor with 640×480

72 pixels of 5.6 μm size, one pixel corresponding to 100 μm in the image field, read
73 out by a 10 bit ADC whose most significant 8 bits encode the CCD output signal.

74 In order to test how the performance depends on the components of the existing
75 system, a second converter screen, named scintillator 2 in the following, and a
76 different CCD camera were also tested. The converter has the same composition
77 as scintillator 1, embedded in a stable plastic matrix, and has a total thickness of
78 450 μm . The CCD camera is a Manta G-032B (Allied Vision Technology)
79 equipped with the same optical system of $f=16$ mm and $F/1.4$. The CCD sensor is
80 a Sony ICX424 with 656x492 pixel of 7.4 μm size, one pixel corresponding to
81 100 μm in the image field, read out by a 12 bit ADC.

82 An x-y translator, positioned inside the sample tank, is available for sample
83 alignment [6]. A precision rotary stage (Newport URS150-BPP) was added to the
84 existing setup to perform a neutron tomography.

85 In order to test the diagnostic potential of the apparatus on metal artifacts, test
86 samples were prepared by the INFN (National Institute of Nuclear Physics)
87 mechanical workshop in Torino. The densities and material compositions of these
88 samples are reported in Table 1.

89 In particular, to probe the imaging capabilities of the apparatus as a function of
90 material composition and thickness, three step wedges of steel, brass and
91 quaternary bronze alloy were prepared (figure 1 a). These three materials were
92 chosen as they constitute by far the most common metal alloys used in the past for
93 cultural artifacts. Each step is a square of 10x10 mm^2 with a thickness
94 incrementing in each step by 2 mm, from 2 mm up to a maximum of 30 mm. In
95 addition, to investigate the capability of neutron tomography of metal alloy
96 objects, a 25 mm edge bronze cube (figure 1 b) was built to fit in the spot size of
97 the INES neutron beam. The cube faces are held together by means of screws and
98 welds and have a thickness of 4 mm, reduced to 2 mm for two opposite side faces,
99 to mimic the typical bronze thicknesses of statues. Two circular holes of 1 mm
100 diameter were added on one of the two thinner faces to simulate air bubbles and
101 three square base rods, 3x3x15 mm^3 size, two made of steel and one of aluminum,
102 were inserted in the central part to simulate the presence of inner structures.

103 **3. Results**

104 The two scintillator screens coupled with both the CCD cameras were tested in
105 order to determine the linearity, the signal-to-noise ratio, the effective dynamic
106 range and the spatial resolution separately for all the combinations. Later, the best
107 combinations were used to analyze the metallic test samples.

108

109 **3.1 Linearity**

110 For this, a set of images of the light emitted by the converter screen illuminated by
111 the open neutron beam was collected for increasing exposure times to simulate the
112 behavior with increasing signal intensities. A square region of interest (ROI) of
113 10x10 pixels, corresponding to an area of approximately 1 mm² of the image
114 field, was selected in the central area of the images, where the neutron beam is
115 uniform, and was used to calculate the average ADC value (or gray level) and its
116 standard deviation (or noise). These quantities are derived with the assumption
117 that the pixels gray level fluctuations in the ROI of a single image are equivalent
118 to the gray level fluctuations of a single pixel in a sequence of identical images.

119 The measurements with the DMK camera, with both the scintillator screens, were
120 performed by setting the electronic gain to 24.6 dB (available range is 0 - 36 dB)
121 and increasing the exposure times up to the maximum allowed of 30 s. Similar
122 measurements with the Manta camera were performed setting the electronic gain
123 to 15 dB (available range is 0 dB- 36 dB) and increasing the exposure time up to
124 the maximum available of 60 s. The results are shown in figure 2 and 3 where the
125 gray levels are displayed as a function of the exposure time. It should be noticed
126 that, at the maximum exposure time, the signal range of the DMK camera covers
127 only about one half of the available 256 gray levels. On the contrary, at the
128 maximum exposure time, the Manta camera reaches with the scintillator 2 the
129 saturation level of 4095; this value is therefore not included in the analysis.

130 The data indicate a good linearity of the imaging systems as resulting from the fits
131 to a straight line shown in the figures 2-3, the maximum deviation from linearity
132 being 1 gray level for DMK with both scintillators and 25 and 12 gray levels for
133 Manta with scintillator 1 and scintillator 2 respectively. In addition, the slope of
134 the fit for the thicker converter, scintillator 2, is always larger, as expected as a
135 consequence of the larger conversion efficiency. For a fixed exposure time this

136 leads to a slightly larger effective dynamic range, as will be shown in the
137 following section.

138

139 **3.2 Effective dynamic range**

140 First the signal-to-noise ratio was studied, where the signal and the noise were
141 determined for increasing exposure times as described in the previous section. It is
142 found that, for all the different setup configurations, the signal-to-noise ratio as a
143 function of the gray level signal can be approximated by a power curve with a
144 fractional exponent; an example it is shown in figure 4 for the Manta camera
145 coupled with scintillator 2. This behavior indicates that the dominant contribution
146 to the noise is originated from the statistical fluctuations in the number of photons
147 hitting the CCD cells and thus increases with the signal level; in fact, assuming a
148 pure Poisson statistical process, the signal-to-noise ratio should behave like a
149 power function with exponent equal to 0.5.

150 In order to compare the effective dynamic range of the different combinations of
151 camera and converter, the method described in [8] was used. The effective
152 dynamic range can be expressed as the number of effective distinguishable gray
153 levels L of the system, depending on both the signal s and the noise $N(s)$, through
154 the formula

$$155 \quad L = \int \frac{ds}{N(s)} \quad (1)$$

156 where the integration is performed over the useful signal range. Since this range
157 increases with the exposure time and given the poissonian nature the noise, the
158 comparison should be performed for equal exposure times, i.e. for equal number
159 of neutrons hitting the converter, and the signal integration ranges should be
160 chosen accordingly.

161 As an example, figure 5 shows $1/\text{noise}$ as a function of the gray level for the same
162 camera and scintillator of figure 4. For each scintillator-camera combination the
163 data were fitted with a power function and, for each exposure time, the result was
164 integrated from dark signal (8.33 and 9.13 gray levels for DMK and Manta
165 respectively) up to the measured signal level shown in the figures 2 and 3.

166 The results are shown in figure 6 where the effective number of gray levels L is
167 represented as a function of the exposure time. For each exposure time the
168 scintillator 2 is providing a slightly better dynamic range than the scintillator 1

169 and so does the Manta camera compared to the DMK. The best combination is
 170 found to be the Manta CCD camera coupled with scintillator 2 which reaches
 171 about 80 effective gray levels before saturation. On the contrary the present INES
 172 imaging system comprising the DMK camera is limited in dynamic range mainly
 173 because of the shorter maximum exposure time of the camera. Table 2
 174 summarizes the maximum dynamic ranges, corresponding to the maximum
 175 exposure time before saturation, expressed for all the combinations both in terms
 176 of effective number of gray levels L and in dB through the formula

$$177 \quad D(\text{dB}) = 20 \log L \quad (2)$$

178 It should be observed that even if these results were obtained in a limited central
 179 area of the image of 1 mm^2 , their validity can be extended to the entire beam
 180 active area as the maximum non-uniformity was measured to be below 1% (5%)
 181 sampling a region of 1 mm^2 in a central area of $24 \times 24 \text{ mm}^2$ ($35 \times 35 \text{ mm}^2$).

182

183 **3.3 Spatial resolution**

184 The spatial resolution of the radiographic system was evaluated by analyzing the
 185 image of a high contrast sharp edge, realized with a Gadolinium slab, in terms of
 186 the Edge Spread Function (ESF) and the Modular Transfer Function (MTF) [9].

187 The edge was placed at around 10 cm far from the scintillator in order to
 188 reproduce the measurement conditions required in the tomography set-up. Since
 189 the Gd slab was not perfectly aligned with the CCD, the sharp edge image was
 190 fitted with a modified Cauchy functional form:

$$191 \quad \varphi(x, y)_{a,b,\beta,\lambda,x_0} = a \left\{ \frac{1}{2} + \frac{1}{\pi} \arctan[\lambda(x - \beta y - x_0)] \right\} + b \quad (3)$$

192 where a and b are constants, x and y are the coordinates in the image plane, x_0 is
 193 the edge position, β is the edge slope and λ is a parameter related to the full width
 194 half maximum (FWHM) of the ESF derivative. In fact it can be shown that

$$195 \quad \text{FWHM} = \frac{2}{\lambda} \cos(\tan^{-1} \beta) \approx \frac{2}{\lambda} \left(1 - \frac{\beta^2}{2} \right) \quad (4)$$

196 where the last approximation is valid for small values of β .

197 The spatial resolution FWHM obtained with this method for all combinations of
 198 CCD cameras and scintillators is summarized in Table 3.

199 The corresponding MTF was obtained from the ESF derivative by Fourier
 200 transform and the spatial frequency corresponding to the MTF value of 0.1 was

201 considered as the spatial resolution of the imaging system in lp/mm. The results
202 are summarized in Table 4.

203 As expected, the scintillator 1, being thinner than scintillator 2, shows a better
204 spatial resolution. It is also found that the spatial resolution of the Manta camera
205 appears worse than with the DMK; this can be partially explained by considering
206 that the optical system used for the experiment was specifically optimized for the
207 use with the DMK camera.

208

209 **3.4 Study of the test samples**

210 In order to test the imaging capabilities of the apparatus as a function of metal
211 type and thickness, neutron radiographies of the three step wedges made of steel,
212 brass and quaternary bronze alloy were acquired. Additional dark and open beam
213 images were acquired for later correction. Only the Manta CCD camera coupled
214 with scintillator 2 was used in order to exploit the highest effective dynamic
215 range. Images were acquired setting the integration time to 45 s to avoid
216 saturation effects, and the electronic gain to 15 dB.

217 To reduce the randomly distributed noise due to scattered gamma rays, the raw
218 images were processed with a radius 3 median filter [10]. The final positive
219 radiographic image (I_F) was obtained by subtracting from the raw image (I) the
220 dark image (D) and normalizing to the beam image (B) to correct for the
221 inhomogeneities of the beam, according to the formula:

$$222 \quad I_F = \frac{(I) - (D)}{(B) - (D)} \quad (5)$$

223 Figure 7 shows the radiographic image of the three step wedges and the
224 corresponding gray level profiles, calculated averaging over 20 rows of pixels in
225 the centre of the wedge. Here, zero level corresponds to complete absorption
226 (black) and one to no absorption (white). Given the good linearity of the system,
227 the profiles can also be interpreted as neutron beam intensity profiles. As
228 expected, for all the three wedges, the gray level of each step decreases with the
229 increase of the thickness (right to left in the figure), up to the largest thickness
230 where the noise contribution starts to dominate. It can be deduced from this figure
231 that only those metallic art objects having a metal thickness not exceeding 30 mm
232 can be conveniently investigated with this system. The separation among the three
233 profiles originates from the differences of the neutron cross sections for the

234 different wedge materials. For reference, figure 8 displays the total cross sections
235 of the three constituent materials as a function of the neutron energy calculated
236 with the MCNP4C2 simulation code [11] in the INES neutron energy range (7.8
237 meV – 5 eV). Such a difference in the cross section, combined with a 3D
238 tomographic reconstruction, could be exploited to differentiate the constituting
239 metal of hidden parts of the object.

240 Figure 9 shows, for each of the three wedges, the attenuation of the neutron beam
241 as a function of the thickness of the wedge step. Since the intensity I of a neutron
242 beam traversing a material thickness x is attenuated according to the exponential
243 law $I = I_0 e^{-\Sigma x}$, it is possible by performing a fit to extract the macroscopic cross
244 section Σ separately for the three materials. Table 5 shows the results in terms of
245 cross section over density (Σ/ρ) compared to the predictions obtained by
246 processing the ENDF/B VI microscopic cross sections with the MCNP4C2 code
247 and extracting the expected Σ at the neutron beam energy of 1 eV; this energy
248 corresponds to the average of the INES beam energy spectrum at the sample
249 position [3]. The agreement is found to be satisfactory within the statistical
250 uncertainty.

251 Finally, in order to investigate the potential of neutron tomography on metal alloy
252 objects, a tomography of the bronze cube was performed. Here the DMK camera
253 and the scintillator 1 were used as they showed to provide the best spatial
254 resolution. The cube, placed 10 cm far from the scintillator screen, was rotated by
255 angular steps of 0.7° up to a total of 179.9° and a projection was acquired at each
256 angular position using an exposure time of 16 s.

257 To perform the 3D volume reconstruction, the algorithm of Filtered Back-
258 Projection (FBP), developed for X-ray tomography and implemented in the
259 *Imgrec* software [12], was used. Parallel beam geometry was assumed which
260 allows the reconstruction using projections over 180° [13].

261 The tomography of the cube proved the possibility to resolve details at a
262 millimetric scale inside metal structures. Figure 10 shows a horizontal section and
263 a 3D rendering of the cube. Welds and holes are clearly visible in the horizontal
264 section. Note that in the figure the aluminum column is invisible as the aluminum
265 cross section is about one order of magnitude lower than steel cross section.
266 However, changing the gray level threshold, the 3D rendering of the cube worsens
267 but the aluminum column becomes visible.

268 **4. Conclusions**

269 Series of measurements were performed to characterize the imaging capabilities
270 of the INES setup for objects of interest in the cultural heritage field. Different
271 combinations using a thicker scintillator screen and a different CCD camera with
272 a larger maximum bit depth were also tried to find possible improvements to the
273 existing system.

274 For all the combinations a good linearity of the imaging system was obtained.
275 The best dynamic range of about 80 effective gray levels was obtained with a
276 Manta 12 bit CCD camera coupled with the thicker scintillator. On the contrary
277 the present INES imaging system, comprising a DMK 8 bit CCD camera and the
278 thinner scintillator, was limited to about 43 effective gray level mainly because of
279 the short maximum exposure time of this camera. However this combination
280 showed the best spatial resolution of 182 μm (FWHM), corresponding to 4.0
281 lp/mm.

282 The combination featuring the best dynamic range was used to investigate the
283 imaging capabilities for metal alloy objects as a function of the metal thickness
284 and alloy composition. For this purpose, three step wedges made of steel, brass
285 and bronze were analyzed, showing that the investigation of metallic objects up to
286 a thickness of about 30 mm can be achieved at this facility. The neutron
287 attenuation coefficients for the three metal alloys were also measured from the
288 attenuation curves and compared with the predictions of the ENDF/BVI library,
289 showing a good agreement.

290 Finally, the tomography of a hollow bronze cube with wall thicknesses in the
291 range 2-4 mm, typical of the bronze statues, and with inner insertions of steel and
292 aluminum parts, was carried on using the present INES setup in order to exploit
293 the best spatial resolution. The results showed that the presence of metallic
294 structures inside the bronze shell can be easily revealed with this technique, and
295 that holes and welding material at a millimetric scale can be revealed.

296 **Acknowledgements**

297 This study has been carried out in the framework of the “neu_ART” research project funded by
298 Regione Piemonte. The use of the spallation neutron source ISIS (UK) was made possible by the
299 Cooperation Agreement no. 06/20018 between CNR and STFC.

300 **References**

301 1 Lehmann E H et al. Nuclear Instruments and Methods in Physics Research A “Non-invasive
302 studies of objects from cultural heritage” (2005), 542 68–75.

303 2 Lehmann E H et al. Archaeometry “Investigation of the content of ancient Tibetan metallic
304 Buddha statues by means of neutron imaging methods” (2010) 52, 3:416-428.

305 3 Grazzi F et al. Nuovo Cimento “Preliminary results of the Italian neutron experimental station
306 INES at ISIS: Archaeometric applications” (2007) 30 59-65.

307 4 Bartoli L et al. Nuclear Instruments and Methods in Physics Research A “Test measurements
308 with a new imaging alignment camera at ISIS” (2008) 595, 643-646.

309 5 Salvato G et al. Nuovo Cimento “Neutron Tomography at INES: first experimental results”
310 (2008) 31 C, N. 4.

311 6 Grazzi F et al. Review of Scientific Instruments “A neutron imaging device for sample
312 alignment in a pulsed neutron scattering instrument” (2009) 80 1-4.

313 7 Data provided by the material supplier.

314 8 Bettuzzi M et al. Proceedings of SPIE “Effective dynamic range measurement for a CCD in full-
315 field industrial X-ray imaging applications” (2007) 6616 66161L.

316 9 Hall E L “Computer image processing and recognition” (1979) Academic Press, New York.

317 10 <http://rsb.info.nih.gov/ij/>

318 11 Briesmeister J F E “MCNP—a general Monte Carlo N-particle transport code” Version 4C,
319 LA-13709 (2000) Los Alamos National Laboratory Report.

320 12 Developed by D Schneberk at Lawrence Livermore National Laboratory, see also Martz H E et
321 al. “X-ray Imaging” (2009) CRC Press Inc, Bosa Roca.

322 13 Kak A C and Slaney M “Principles of Computerized Tomographic Imaging” (1988), IEEE
323 Press.

324

325

326

327

328

329

330

331

332

333

334

335

336

337 **Figures Captions**

338 **Fig. 1** The three step wedges (a) and the bronze cube (b).

339

340 **Fig. 2** DMK camera: linearity of the signal as a function of the exposure time.

341

342 **Fig. 3** Manta camera: linearity of the signal as a function of the exposure time.

343

344 **Fig. 4** Manta camera: signal to noise ratio as a function of the gray level signal.

345

346 **Fig. 5** Manta camera: 1/noise as a function of the gray level.

347

348 **Fig. 6** Effective number of gray levels as a function of the exposure time for the four different
349 combinations of camera and converter.

350

351 **Fig. 7** Neutron radiography of the three step wedges (above) and corresponding neutron absorption
352 profiles (below). The upper scale of the plot indicates the step thickness.

353

354 **Fig. 8** Total neutron cross sections of the constituent materials of the step wedges calculated with
355 MCNP4C2 simulation code.

356

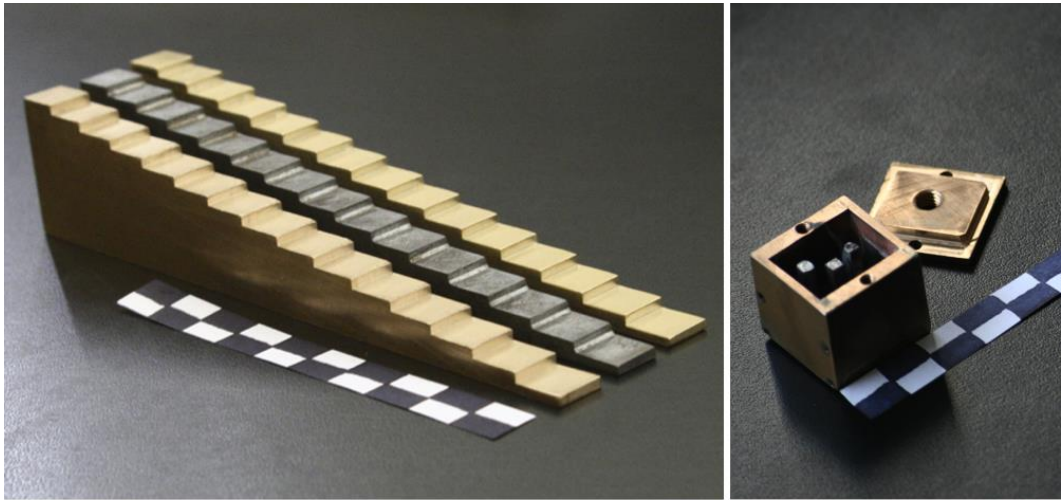
357 **Fig. 9** Neutron attenuation curves for the three wedges as a function of the step thickness.

358

359 **Fig. 10** Cube phantom tomography reconstruction: section (a) and 3D rendering (b).

360

361 **Figure 1**



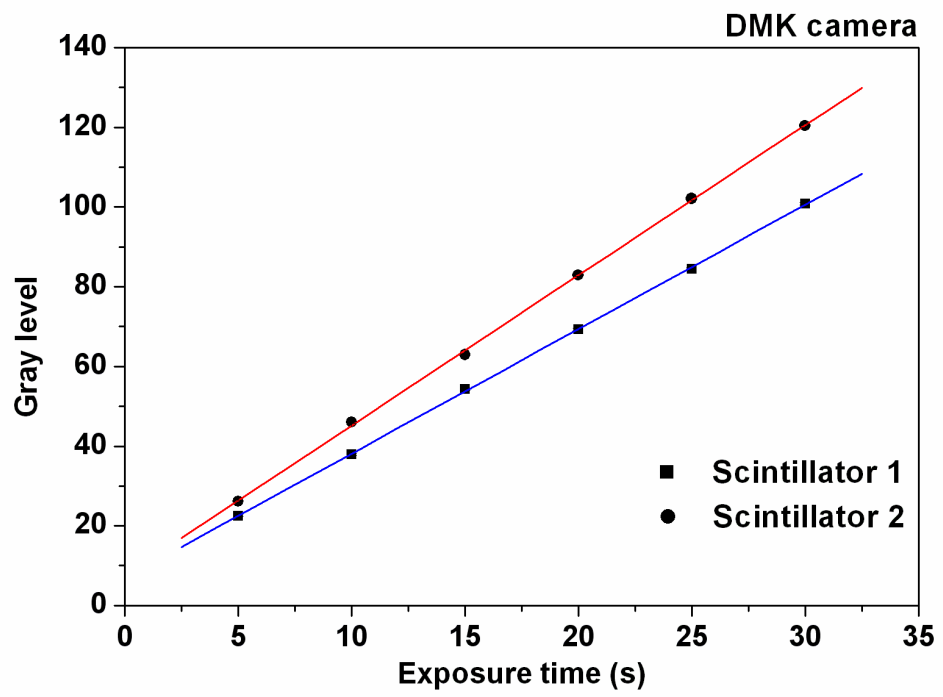
(a)

(b)

362

363

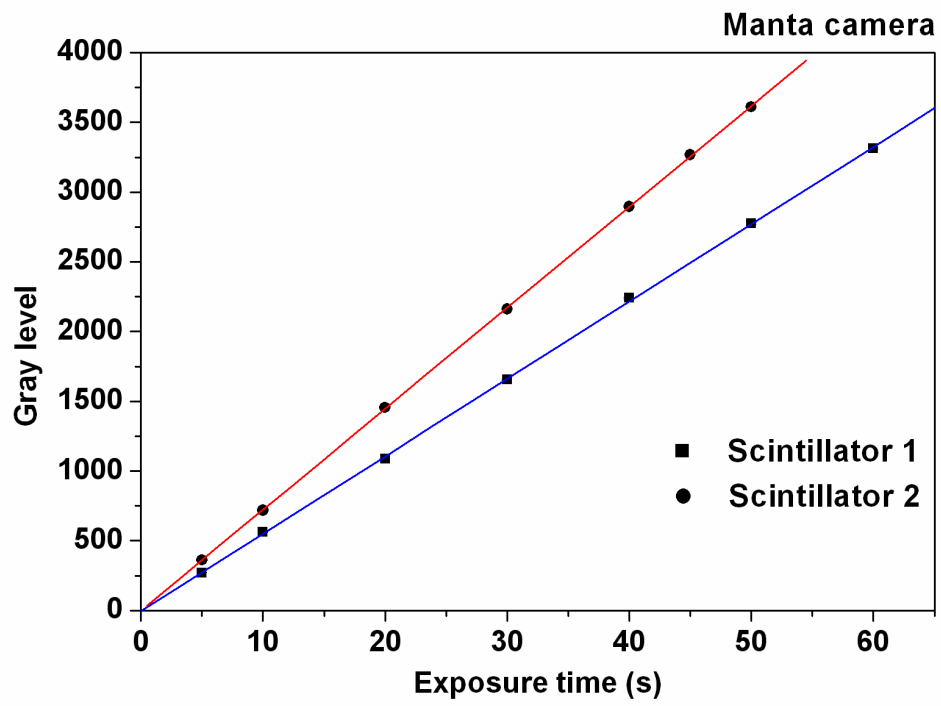
364 **Figure 2**



365

366

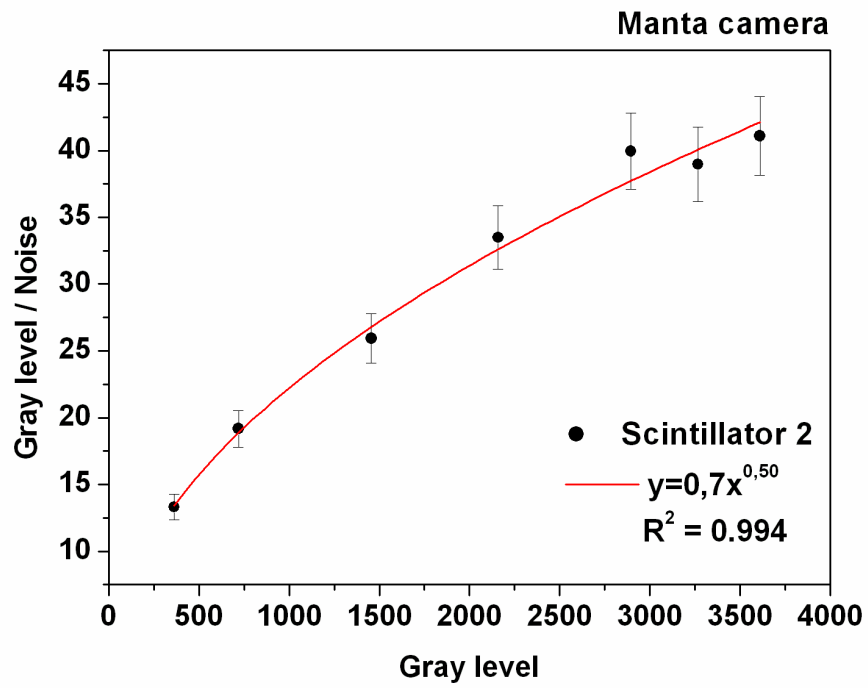
367 **Figure 3**



368

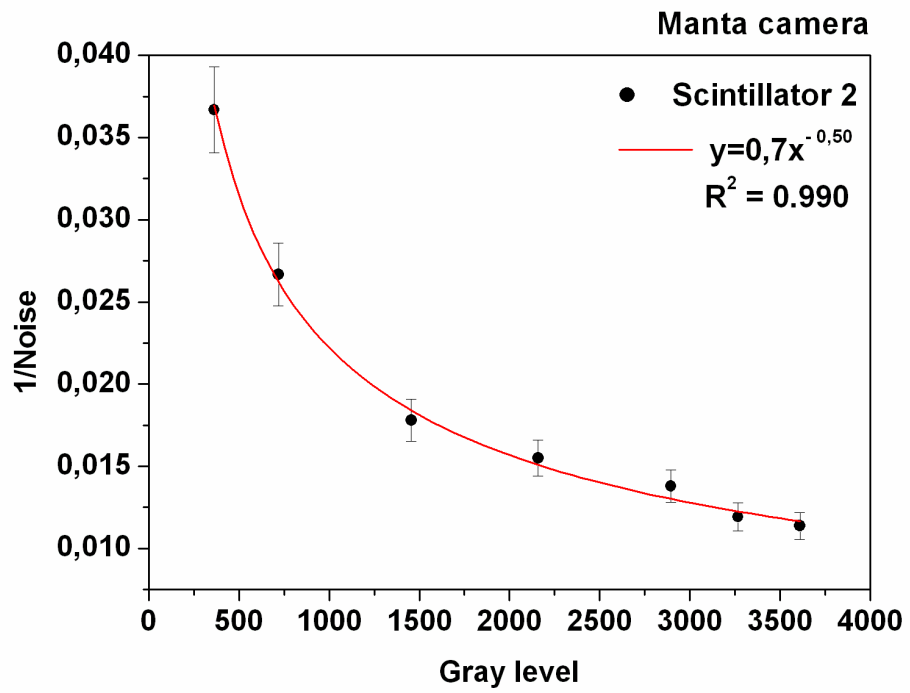
369

370 **Figure 4**



371

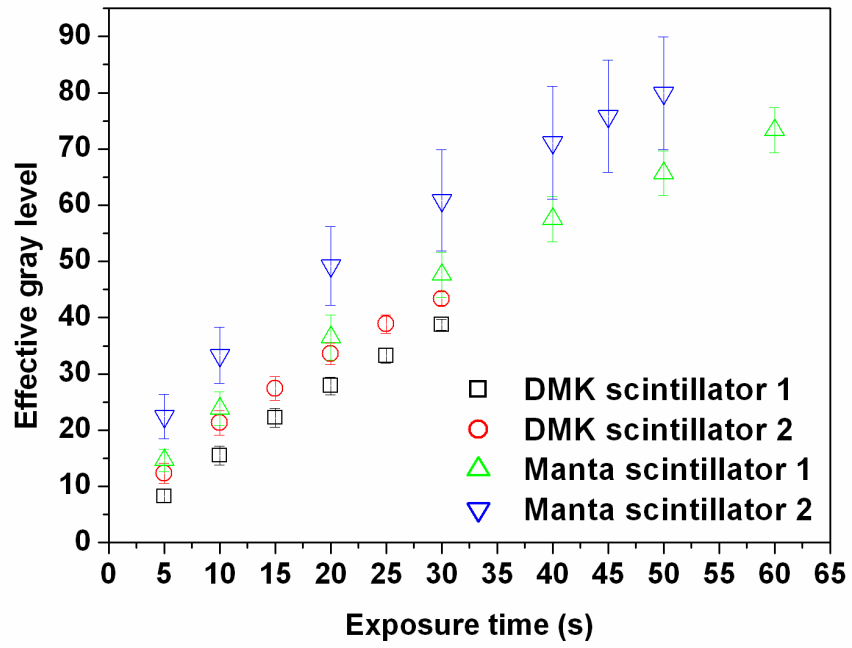
372 **Figure 5**



373

374

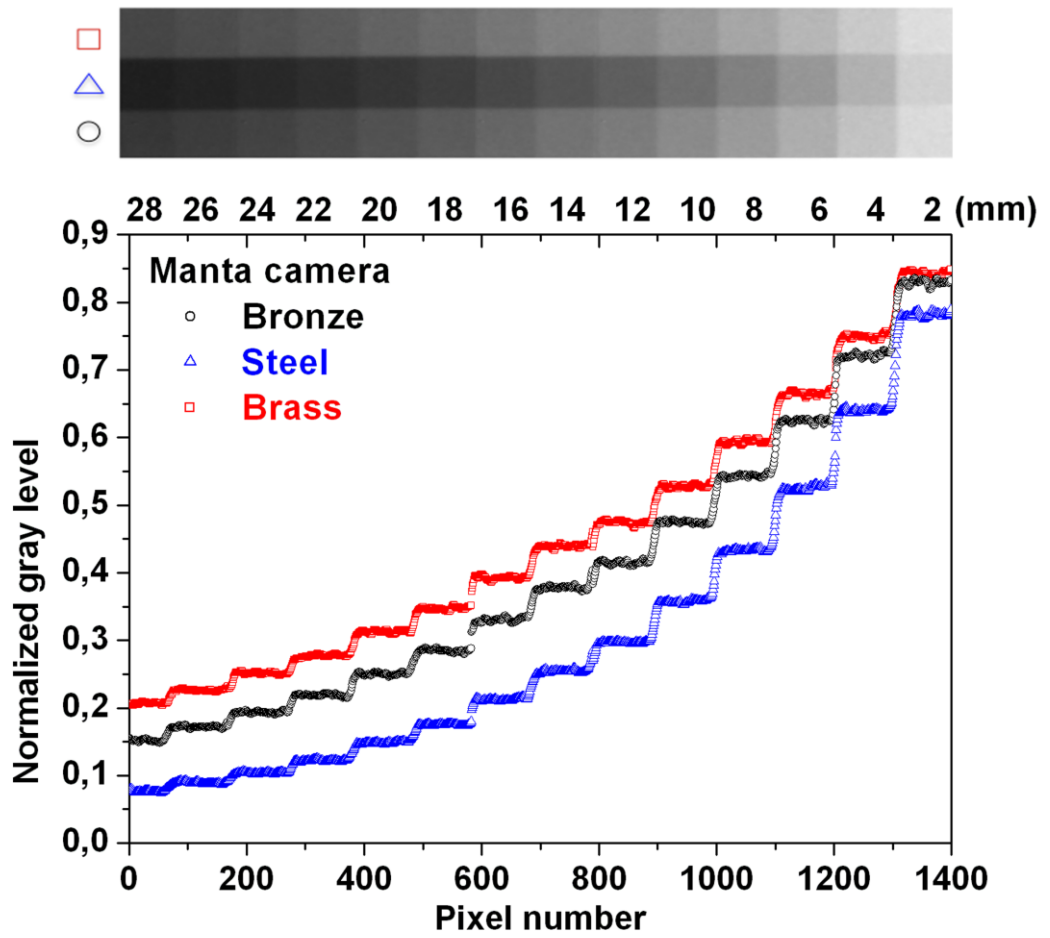
375 **Figure 6**



376

377

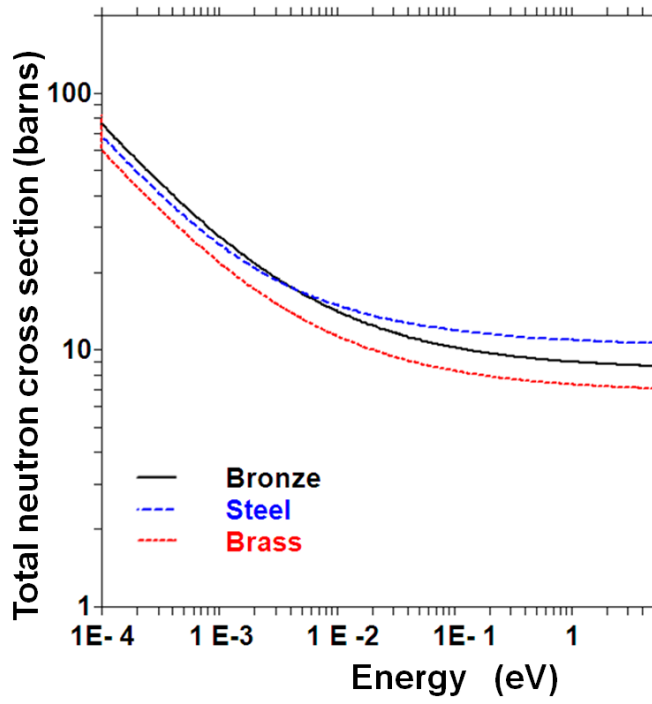
378 **Figure 7**



379

380

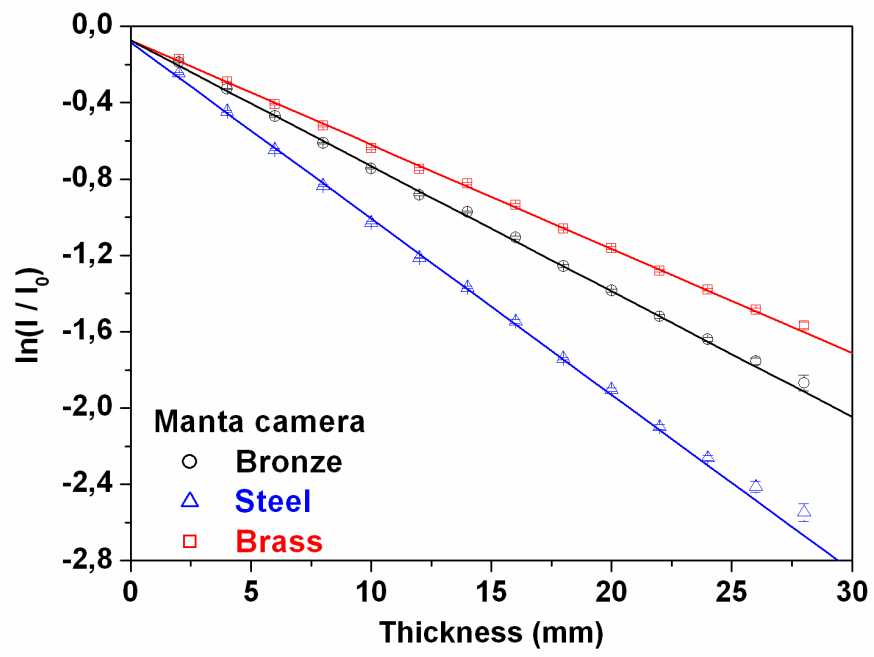
381 **Figure 8**



382

383

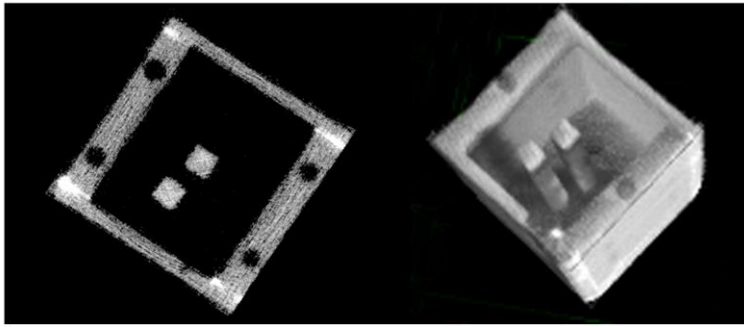
384 **Figure 9**



385

386

387 **Figure 10**



(a)

(b)

388

389

390

391 Table1: Samples density and elemental composition [7].

392

Material	Density [g cm ⁻³]	Elemental composition
C40 carbon steel	7.85	Fe; C (0.38-0.43%); Si (0.15-0.35%); Mn (0.6-0.8%); P (max 0.02%); S (max 0.008%); Cr (0.15-0.35%)
Turning brass	8.29	Cu; Zn (39%); Pb (3%)
Bronze (85-5-5-5)	8.88	Cu; Pb (5.81%); Sn (5.05%); Zn (5.46 %); Fe (0.11%); Ni (1.21%); Al (trace)

393

394

395

396 Table 2: Maximum effective dynamic range in terms of effective number of gray
397 levels and in dB.

	DMK		Manta	
Scintillator 1	39±2	(31.8±0.4) dB	73±4	(37.3±0.5) dB
Scintillator 2	43±1	(32.7±0.2) dB	80±10	(38.1±1.1) dB

398

399

400

401 Table 3: Spatial resolution, defined as FWHM of the ESF derivative, measured for
402 both cameras coupled with both scintillators.

FWHM (μm)	DMK	Manta
Scintillator 1	182±11	261±9
Scintillator 2	306±14	389±13

403

404

405 Table 4: Spatial resolution defined as MTF value at 10% calculated for both
406 cameras coupled with both scintillators.

407

MTF 10% (lp/mm)	DMK	Manta
Scintillator 1	4.0±0.2	2.74±0.10
Scintillator 2	2.37±0.11	1.84±0.06

408

409 Table 5: Σ/ρ values obtained with Manta CCD camera compared to the
410 predictions.

411

Material	ρ (g cm ⁻³)	Measured Σ/ρ (cm ² g ⁻¹)	ENDF/B-VI Σ/ρ @1 eV (cm ² g ⁻¹)
Steel	7.85	(11.9±0.4) 10 ⁻²	12.02 10 ⁻²
Brass	8.29	(6.6±0.2) 10 ⁻²	6.64 10 ⁻²
Quaternary bronze alloy	8.88	(7.4±0.2) 10 ⁻²	7.24 10 ⁻²

412

413